PHYSICAL REVIEW B **112**, 214455 (2025)

Fact and artifact in Lorentz imaging of skyrmionic magnetic textures

Xiaowen Chen,[1,2] Luyan Yang,[3,*] Andrii Savchenko,[4] Donghai Yang,[1] Wen Shi,[2,5] Thibaud Denneulin,[6]
Nikolai S. Kiselev,[4] Lei Jin,[5] Dongsheng Song,[7] Rafal E. Dunin-Borkowski,[6] and Fengshan Zheng[1,2,†]
[1]*Spin-X Institute, School of Physics and Optoelectronics, State Key Laboratory of Luminescent Materials and Devices, Guangdong-Hong Kong-Macao Joint Laboratory of Optoelectronic and Magnetic Functional Materials,*
South China University of Technology, Guangzhou 511442, China
[2]*Center for Electron Microscopy, South China University of Technology, Guangzhou 511442, China*
[3]*Beijing Key Laboratory of Microstructure and Properties of Advanced Materials, College of Materials Science and Engineering,*
Beijing University of Technology, Beijing 100124, China
[4]*Peter Grünberg Institute and Institute for Advanced Simulation, Forschungszentrum Jülich and JARA, 52425 Jülich, Germany*
[5]*Ernst Ruska-Centre for Microscopy and Spectroscopy with Electrons and Peter Grünberg Institute,*
Forschungszentrum Jülich, 52425 Jülich, Germany
[6]*Ernst Ruska-Centre for Microscopy and Spectroscopy with Electrons, Forschungszentrum Jülich, 52425 Jülich, Germany*
[7]*Information Materials and Intelligent Sensing Laboratory of Anhui Province, Key Laboratory of Structure and Functional Regulation of Hybrid Materials of Ministry of Education, Institutes of Physical Science and Information Technology, Anhui University, Hefei 230601, China*

(Received 2 August 2025; revised 1 November 2025; accepted 16 December 2025; published 30 December 2025)

Lorentz transmission electron microscopy is widely used for imaging magnetic structures at the nanoscale in real space. However, its interpretation can be complicated by imaging artifacts induced by the defocus distance and specimen tilt. In this work, we systematically examine the origins of such artifacts through experimental and simulated Fresnel defocused Lorentz imaging of Bloch-type skyrmionic spin textures. We analyze the effects from the defocus distance, the magnetic field, and the sample thickness in an individual skyrmion, two neighboring skyrmions, and the skyrmion lattice. We demonstrate that improper defocus distance and specimen tilt may introduce artifacts that are not associated with the actual magnetic configurations. These findings provide a practical framework for Lorentz TEM imaging and highlight the importance of the defocus distance, sample tilt, and theoretical support for reliable interpretations of magnetic textures.

DOI: 10.1103/sm5r-2vps

I. INTRODUCTION

A variety of characterization techniques have been used to study nanoscale magnetic structures in materials, including neutron scattering [1], magnetic force microscopy [2], magneto-optical Kerr microscopy [3], x-ray microscopy [4] and Lorentz imaging [5], off-axis electron holography [6], and differential phase contrast (DPC) imaging [7] in the transmission electron microscope (TEM). In particular, Fresnel defocused imaging in Lorentz TEM is a widely used technique that enables the measurement of projected in-plane magnetic induction with nanometer-scale spatial resolution in real space [8,9]. It has been utilized to verify the existence of topological solitons in magnetic materials, for example, bubbles [10], skyrmions [11], antiskyrmions [12,13], biskyrmions [14], bobbers [15], merons [16], and hopfions [17].

In the Fresnel defocused imaging mode of Lorentz TEM, the image contrast is primarily governed by the projected magnetic vector potential along the electron beam direction, both within and beyond the sample. This fundamental mechanism complicates the direct interpretation of Lorentz TEM images, especially for systems with complex three-dimensional (3D) spin textures, improper imaging conditions, or sample geometry (e.g., nonflat or tilted specimens). For example, type II magnetic bubbles could be misinterpreted as biskyrmions [18,19], and Néel-like structures remain invisible at zero specimen tilt due to the cancellation of vector potential components along the electron beam direction [9,20,21]. Furthermore, Lorentz TEM contrast cannot distinguish magnetic chirality [22], and artifacts may arise from sample tilting [23] or improper applications of the transport of intensity equation (TIE) during phase retrieval [19,23], as well as from the Fresnel fringes from sample edges or interfaces. Such misinterpretations can obscure the true topology of magnetic textures, hinder the identification of spin chirality, and potentially lead to incorrect conclusions about statics and dynamics of magnetic structures.

In this work, we investigate the origins and manifestations of imaging artifacts in Lorentz TEM of skyrmionic magnetic textures. We focus in particular on the influence of the defocus distance and the specimen tilt on the imaging of Bloch-type skyrmions. Our findings highlight the importance of careful interpretation of the Lorentz TEM contrast, and we provide experimental and simulated evidence to guide accurate imaging and analysis of these topological magnetic structures.

---

[*] Contact author: yangluyan@bjut.edu.cn

[†] Contact author: zhengfs@scut.edu.cn

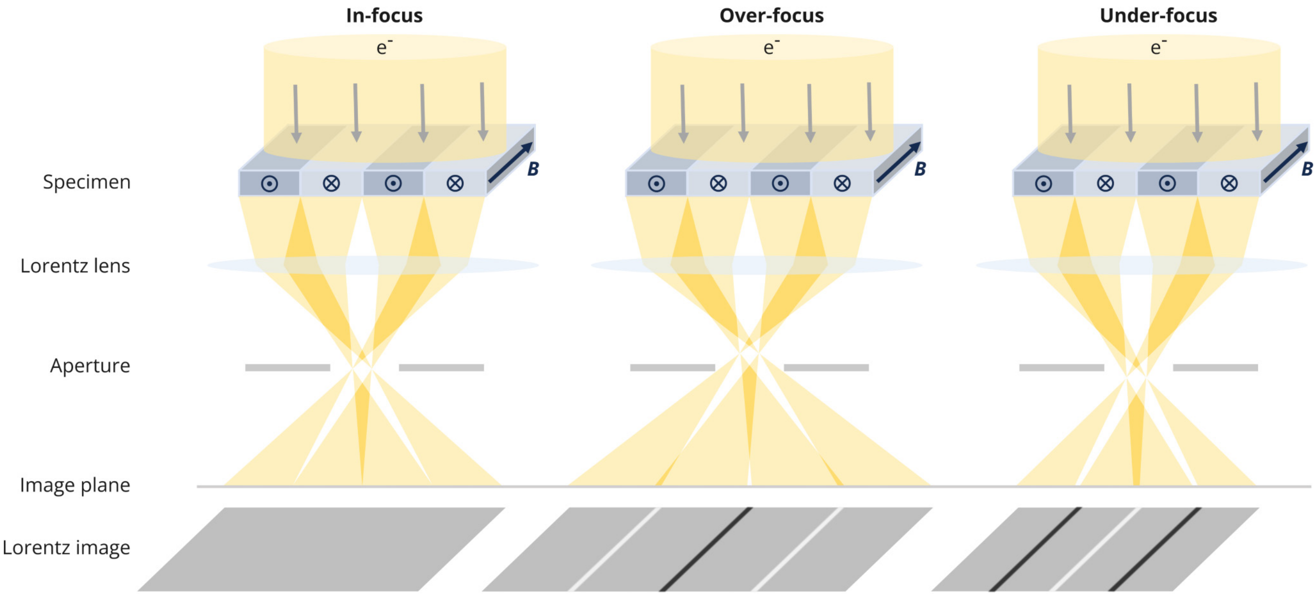

FIG. 1. Schematic of Fresnel defocused Lorentz TEM imaging at in-focus, over-focus, and under-focus conditions.

II. FUNDAMENTAL PRINCIPLE

When an electron beam passes through a magnetic sample, it experiences a Lorentz force arising from interactions with both electrostatic and magnetic fields. To first-order approximation, it is thus assumed the image contrast is associated with the in-plane magnetic induction projected along the electron beam direction. A simplified model of Lorentz magnetic imaging is illustrated in Fig. 1. In the in-focus condition, no magnetic contrast is observed. When acquired under defocused conditions, i.e., under- or over-focus, the Lorentz TEM image reveals bright or dark contrast in association with magnetic features, thereby enabling the qualitative visualization of domain walls.

In the presence of electrostatic (V) and magnetic vector ($\mathbf{A}$) potentials, the phase shift ϕ of the electron wave is governed by the Aharonov-Bohm effect [24] and can be formulated:

$$\phi(\mathbf{r}_\perp) = C_E \int_{-\infty}^{+\infty} V(\mathbf{r}_\perp, z)dz - \frac{e}{\hbar}\int_{-\infty}^{+\infty} \mathbf{A}(\mathbf{r}_\perp, z)dz, \quad (1)$$

where e and $\hbar$ are the elementary electron charge and the reduced Planck constant, respectively, $\mathbf{r}_\perp$ denotes the lateral dimensions in the sample plane and z is the electron beam direction, C_E is the interaction constant that depends on the electron energy. For 300 keV electrons, $C_E = 6.53 \times 10^{-3}$ rad V^{-1} nm^{-1}. Note that only the z component of the magnetic vector potential ($\mathbf{A}_z$) contributes to the phase shift. Phase contrast techniques in the TEM can directly or indirectly measure this phase shift, such as electron holography, Fresnel defocused imaging via the TIE, DPC imaging and electron ptychography in scanning transmission electron microscopy. However, TIE and iDPC may suffer from artifacts due to undefined boundary conditions and numerical errors.

Here we briefly review the image formation mechanism in conventional TEM, which also applies to Fresnel defocused Lorentz imaging. Refer to textbooks for more details, e.g., Refs. [25,26].

Assuming a plane wave for the electron beam in the TEM with a wavelength, λ, an electron-transparent sample modifies both the amplitude (a) and phase (ϕ) of the plane wave, resulting in a wave function (ψ) that can be described as

$$\psi(\mathbf{r}_\perp) = a(\mathbf{r}_\perp)e^{i\phi(\mathbf{r}_\perp)}. \quad (2)$$

In the back-focal plane (BFP) of the Lorentz lens, the wave function is then expressed as

$$\psi(\mathbf{q}_\perp) = \mathcal{F}[\psi(\mathbf{r}_\perp)]\mathcal{T}(\mathbf{q}_\perp), \quad (3)$$

where $\mathcal{F}$ denotes the Fourier transform, $\mathbf{q}_\perp$ is the reciprocal spatial frequency vector in the BFP, and $\mathcal{T}(\mathbf{q}_\perp)$ is the microscope contrast transfer function (CTF). In general, the CTF could be decomposed into three parts: the aperture function $A(\mathbf{q}_\perp)$, the phase transfer function $e^{-i\chi(\mathbf{q}_\perp)}$, and the damping envelope function $e^{-g(\mathbf{q}_\perp)}$. The CTF can thus be written in the form

$$\mathcal{T}(\mathbf{q}_\perp) = A(|\mathbf{q}_\perp|)e^{-i\chi(\mathbf{q}_\perp)}e^{-g(\mathbf{q}_\perp)}. \quad (4)$$

The aperture function is equal to one inside the aperture and zero outside. $\chi(\mathbf{q}_\perp)$ is usually determined by the defocus Δf and the spherical aberration of the Lorentz lens C_s in Fresnel Lorentz imaging. It can thus be formulated as

$$\chi(\mathbf{q}_\perp) = \pi\lambda\Delta f {\mathbf{q}_\perp}^2 + \frac{\pi}{2}C_s\lambda^3{\mathbf{q}_\perp}^4. \quad (5)$$

In experiments, $\lambda = 1.97$ pm for 300 kV electrons and C_s is on the order of several hundred millimeters. Since the Lorentz deflection angle from magnetic samples is usually in the order of tens of μrad, which is two or three orders smaller than the Bragg angle, the fourth-order contribution from the spherical aberration of the Lorentz lens can be neglected. Furthermore, twofold astigmatism is assumed to be fully corrected. As such, $\chi(\mathbf{q}_\perp)$ could be simplified:

$$\chi(\mathbf{q}_\perp) = \pi\lambda\Delta f {\mathbf{q}_\perp}^2. \quad (6)$$

The damping envelope $g(\mathbf{q}_\perp)$ is related to microscope stability. Due to the ultra-high-brightness field-emission gun and stable environment in modern microscopes, we can reasonably neglect this term. Thus, in our case, the CTF becomes

$$\mathcal{T}(\mathbf{q}_\perp) = A(|\mathbf{q}_\perp|)e^{-i\pi\lambda\Delta f|\mathbf{q}_\perp|^2}. \tag{7}$$

Finally, the recorded intensity in the image plane can be derived using an inverse Fourier transform:

$$I(\mathbf{r}_\perp) = |\mathcal{F}^{-1}[\psi(\mathbf{q}_\perp)]|^2 = |\psi(\mathbf{r}_\perp) \otimes \mathcal{T}(\mathbf{r}_\perp)|^2, \tag{8}$$

where $\otimes$ is the convolution operation and $\mathcal{T}(\mathbf{r}_\perp)$ is the point spread function for Fresnel Lorentz imaging.

III. EXPERIMENTAL AND NUMERICAL METHODS

Lorentz TEM experiments. TEM specimens were prepared from a single crystal of B20-type FeGe using a lift-out method based on focused-ion beam milling. Fresnel defocused Lorentz TEM imaging was performed using an FEI Titan 60-300 TEM operated at 300 kV. The microscope was operated in Lorentz mode with the sample under magnetic-field-free conditions. The conventional microscope objective lens was then used to apply an out-of-plane magnetic field between −0.15 and 1.5 T, in order to nucleate skyrmions. A liquid nitrogen specimen holder (Gatan Model 636) was used to cool the sample to 250 K for nucleating the skyrmion lattice, and to 100 K for stabilizing isolated and paired skyrmions. Fresnel defocused TEM images were recorded using a 4k × 4k Gatan IS K2 direct electron counting detector, with an exposure time of 2 s.

Micromagnetic simulations. The total energy of the simulated magnetic system includes exchange, Dzyaloshinskii-Moriya interaction (DMI), Zeeman, and demagnetization contributions:

$$\begin{aligned}\varepsilon = &\int_{V_m} \mathrm{d}\mathbf{r}\mathcal{A}|\nabla|\mathbf{m} + \mathcal{D}\mathbf{m}\cdot(\nabla\times\mathbf{m}) - M_s\mathbf{m}\cdot\mathbf{B}\\ &+ \frac{1}{2\mu_0}\int_{R^3}\mathrm{d}\mathbf{r}|\nabla\times\mathbf{A_d}|^2,\end{aligned} \tag{9}$$

where $\mathbf{m}(\mathbf{r}) = \mathbf{M}(\mathbf{r})/M_s$ is the unit magnetization vector, with $M_s = |\mathbf{M}|$ denoting the saturation magnetization. $\mathcal{A}$ is the exchange stiffness constant, $\mathcal{D}$ is the bulk DMI constant, and μ_0 is the vacuum permeability. The total magnetic field is given by $\mathbf{B} = \mathbf{B}_{\text{ext}} + \nabla\times\mathbf{A}_d$, where $\mathbf{A}_d$ represents the magnetic vector potential due to demagnetizing fields. The simulation parameters are based on FeGe [17]: $M_s = 384\times 10^3$ A/m, $\mathcal{A} = 4.75\times 10^{-12}$ J/m, and $\mathcal{D} = 0.853\times 10^{-3}$ J/m^2.

Simulations were carried out on a 256 × 256 in-plane mesh of cubic cells, each with dimensions 2 nm × 2 nm × 2 nm using the high-performance GPU-accelerated software Excalibur [27]. The simulated sample thicknesses were varied depending on the magnetic structures: 120 nm for individual and two neighboring skyrmions and 70, 90, and 180 nm for skyrmion lattices.

Theoretical Lorentz TEM images were calculated from the simulated magnetic structures using Excalibur and the open-source software PyLorentz [28]. Multislice simulations of high-resolution TEM images are performed using the DrProbe software [29].

IV. LORENTZ TEM EXPERIMENTS AND SIMULATIONS OF SKYRMIONIC SPIN TEXTURES

A. Individual and two neighboring skyrmion(s)

Previous reports have clarified the expected behavior of Lorentz TEM contrast as a function of the defocus distance. In the small-defocus limit, the image intensity changes approximately linearly with the defocus distance and reflects the Laplacian of the magnetic phase shift [30]. As the defocus increases beyond this regime, the Fresnel-propagation effects lead to a noticeable broadening of chiral domain-wall contrast, and interference features become more pronounced [31]. These findings provide the theoretical context for the present analysis of skyrmions at experimentally relevant imaging conditions.

Figure 2 presents experimental and simulated Lorentz images of an individual skyrmion and two adjacent skyrmions as a function of the defocus distance. Notably, the skyrmion exhibits radial asymmetry due to the coexistence of cone modulations along the magnetic field and double-twist modulation perpendicular to it [32]. Axial symmetry is recovered only when the cone phase transitions into a fully spin-polarized ferromagnetic state under a sufficiently strong magnetic field. For the isolated skyrmion [Fig. 2(a)], it can be seen that the apparent size of the ringlike contrast increases with the defocus distance. Fresnel fringes take the form of multiple concentric rings around the core at a large defocus. In addition, a larger defocus also introduces asymmetry in the skyrmion contrast. This suggests that a large defocus could introduce imaging artifacts that obscure real magnetic features.

At a small defocus, two neighboring skyrmions can be identified as two individual skyrmions, whereas at a large distance, rings from the two skyrmions interfere with each other [see Fig. 2(b)]. The criterion for the spatial resolution using the Airy disk could be applied here to determine the optimal defocus distance. It is clear that the separation distance between the two skyrmions determines the optimal defocus. This phenomenon should also be expected in the imaging of the skyrmion lattice with a smaller separation distance between adjacent skyrmions (see Fig. 5 below).

To trace the evolution of image contrast with the defocus distance, line profiles of the intensity along the central section of the skyrmions (marked by dashed lines in Fig. 2) are plotted as shown in Fig. 3. For the individual skyrmion [Fig. 3(a)], in the over-focus regime, the profile typically shows a peak, side lobes and extremes (negative maximum) along the radial direction. It can be seen that the position of the intensity peak slightly shifts away from the skyrmion center with increasing defocus distance. In addition, at high defocus distances, the profiles display multiple side lobes and extremes. In the under-focus regime, the profiles instead show a plateau around the center of the skyrmions. Note that there is an asymmetry of the profiles both for the positions and intensities in the left and right side of the skyrmion. Therefore, "1" and "2" are used to mark the left and right sides of the skyrmion, respectively. Similar behavior is also observed in the two-skyrmion case [Fig. 3(b)], while at high defocus distances, profiles are complicated due to the "interference" of the Fresnel fringes of the two skyrmions. The corresponding simulated magnetic isosurfaces are displayed in the insets of

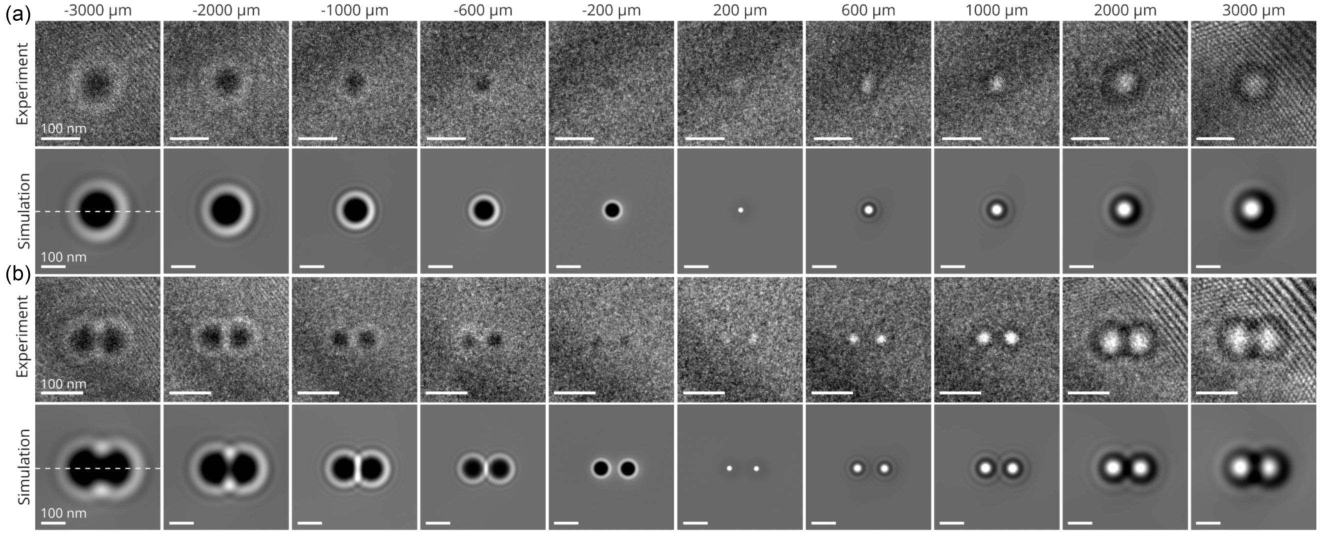

FIG. 2. Representative experimental (top) and simulated (bottom) Lorentz TEM images of (a) an individual skyrmion and (b) two neighboring skyrmions as a function of the defocus distance. The defocus distance is labeled on top of each image in the first row. A gray dashed line for the first simulated Lorentz image in (a) and (b) marks the central axis of the skyrmion. A 600 mT magnetic field is applied perpendicular to the sample. The sample thickness is approximately 120 nm. Images are recorded at a sample temperature of 100 K. Note that there are Fresnel fringes from the sample edges at a large defocus distance, $\geqslant \pm 2$ mm.

Fig. 3. The skyrmion size (R) is the radius of the $m_z = 0$ contour, while W is the skyrmion wall width, following the definitions in Refs. [33,34]. For the individual skyrmion, R is approximately 16.25 nm, and W is about 12.78 nm. For the two-skyrmion configuration, the center-to-center separation between the two skyrmions (L) is approximately 110 nm. According to previous reports [33,35], the skyrmion size decreases with increasing $\mathcal{A}/\mathcal{D}$, with a theoretical value of approximately 35 nm. The skyrmion radius ($R + W$) in our simulations is smaller than the zero-field value predicted by $\mathcal{A}/\mathcal{D}$, due to the slight compression of the skyrmion core by the application of a perpendicular magnetic field of 600 mT. It is worth noting that the actual size and center position of a skyrmion are difficult to determine experimentally and can only be inferred theoretically. However, since a skyrmion is distorted by the magnetic background, it is also difficult to determine the boundary of a skyrmion theoretically.

Detailed analyses of the intensities and positions of the skyrmion peak, the first extreme and the side lobe are provided in Fig. 4. The intensity of the skyrmion peak (open squares) decreases monotonically with the increasing defocus distance in the over-focus regime, while the intensity of the skyrmion peak decreases at a small defocus and then increases at a large defocus distance in the under-focus regime. The intensity for

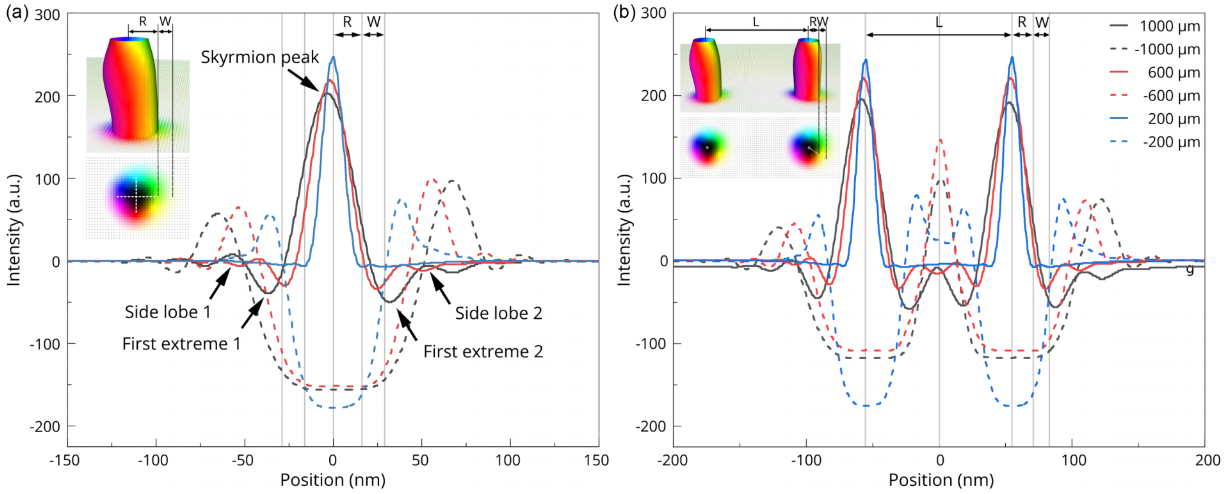

FIG. 3. Representative line intensity profiles of (a) individual skyrmion and (b) two neighboring skyrmions, respectively, extracted along the gray dashed lines in the first simulated Lorentz images of Figs. 2(a) and 2(b). The intensity of the conical phase region was defined as zero. The locations of the skyrmion peak, first extreme and side lobe are marked by arrows in (a). The insets show simulated magnetic isosurfaces illustrating the corresponding 3D spin configurations, with the measurement methods for determining the skyrmion size (R), skyrmion-wall width (W), and skyrmion center separation (L) indicated. The corresponding skyrmion core position, R, W, and L values are also marked in the intensity profiles. The corresponding defocus distances are indicated in the top-right corner in each image.

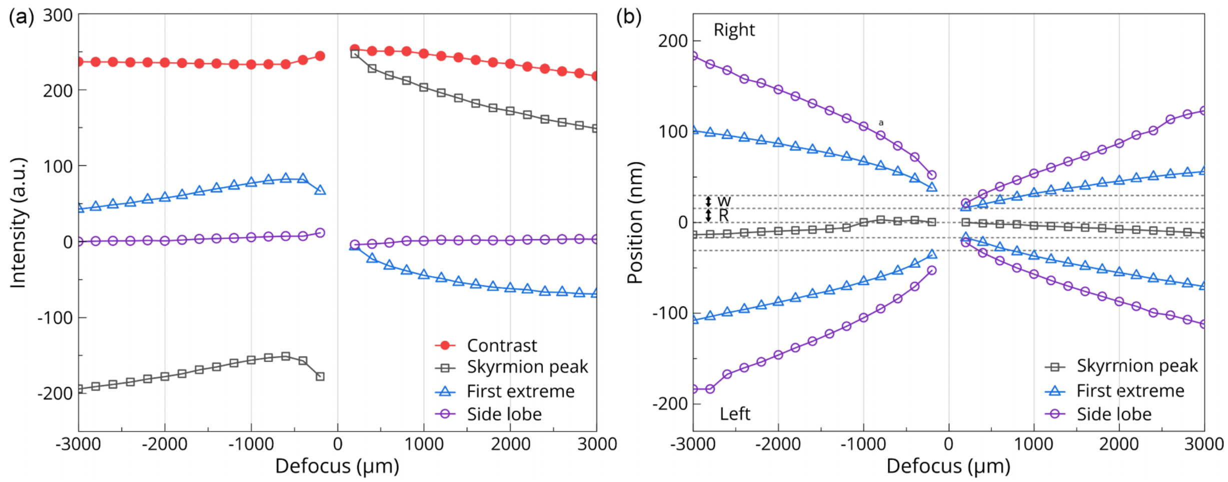

FIG. 4. Analyses of simulated Lorentz TEM images of an individual skyrmion. (a) Intensity profile for the skyrmion peak, first extreme and the side lobe as a function of the defocus distance (open-symbol lines). The three particular points are marked in Fig. 3(a). Contrast profiles for the skyrmion as a function of the defocus distance (red closed circles line). (b) Positions of the three points as a function of the defocus distance. The gray dashed lines mark the skyrmion core, skyrmion size (R), and skyrmion-wall width (W), respectively. "Left" and "Right" on the left side of the image refer to the points 1 and 2 labeled in Fig. 3(a), respectively.

the first extreme (open triangles) shows a similar trend to that of the skyrmion peak. The intensity for the side lobe (open circles) almost stays constant as a function of the defocus distance. Here we define the contrast of the skyrmion to be the intensity difference between the skyrmion peak and the first extreme. It can be seen that the contrast of the skyrmion (closed circles) is slightly larger at a small defocus distance, though it varies in a narrow range from 210 to 250 across the ± 3000 μm defocus distance.

The position of the skyrmion peak almost linearly shifts from the center of the skyrmion in both under- and over-focus regimes (see open squares in Fig. 4), consistent with Fig. 3(a). The observed lateral shift of the intensity peak relative to the skyrmion center originates from the same asymmetry discussed in Fig. 2, namely, the coexistence of cone modulations along the magnetic field and double-twist modulation perpendicular to it [32]. This intrinsic 3D spin configuration leads to a slight imbalance in the projected in-plane magnetic induction, producing a small but measurable contrast displacement in defocused Lorentz images. The positions of the first extreme (open triangles) at -200 μm and $+1000$ μm exactly mark the size of the skyrmion, though shifts farther outside of the skyrmion edges with the increasing defocus distance, except at a smaller ($\leqslant$1000 μm) positive defocus distance, positions of the first extreme fall inside the skyrmion. This may lead to a misjudgement of the actual skyrmion size with under- or over-focus images. Similar behavior is also observed for the positions of the side lobes (open circles).

In summary, due to the asymmetry of the Lorentz TEM images in under- and over-focus regimes, the misalignment between the skyrmion center and maximum intensity (skyrmion peak), it would be misleading to tell the actual central position and size of the skyrmion from Fresnel defocused Lorentz TEM images. Due to dense Fresnel fringes at large defocus distances, and almost constant contrast across a wide range of defocus distances, it would be good to have a small defocus distance for imaging, in particular in the presence of neighboring skyrmions or other magnetic textures, e.g., helical spirals. We then next consider the case where skyrmions are arranged in a regular lattice.

B. Skyrmion lattice

Experimental Lorentz imaging of the skyrmion lattice. While the interference patterns of individual and two neighboring skyrmion(s) reveal key imaging artifacts, more complex behavior arises when skyrmions are arranged in a periodic lattice. For the skyrmion lattice, the apparent size variation with defocus differs from that of an isolated skyrmion, as overlapping Lorentz contrast between neighboring skyrmions modifies the interference pattern and thereby changes the perceived lattice spacing and feature width. Figure 5 presents experimental Lorentz TEM images of a Bloch-type skyrmion lattice in FeGe recorded as a function of defocus distances. It can be seen that as the defocus distance increases, the contrast pattern of the skyrmion lattice changes remarkably.

In the over-focus regime, skyrmions appear as bright circular spots, and the size of this bright spot varies with the increasing defocus, reflecting contrast evolution. At $\Delta f =$ +2500 μm [Fig. 5(f)], a bright line emerges between adjacent skyrmions but disappears at higher defocus. Instead, a new bright spot forms at the center of three neighboring skyrmions at $\Delta f = +3000$ μm [Fig. 5(g)].

In the under-focus regime, the Lorentz contrast of the skyrmion lattice is much more complicated as a function of the defocus. The skyrmion lattice first appears as hexagonal honeycomb disks at a lower defocus distance. As the defocus increases to -1000 μm [Fig. 5(c)], a faint bright spot appears in the center of each disk. At the same time, six bright spots appear around the skyrmion, which merge into continuous bright contours at -1500 μm [Fig. 5(d)]. At -2000 μm, six new peripheral bright spots appear [Fig. 5(e)]. The hexagon formed by these bright spots is rotated by 30° relative to the

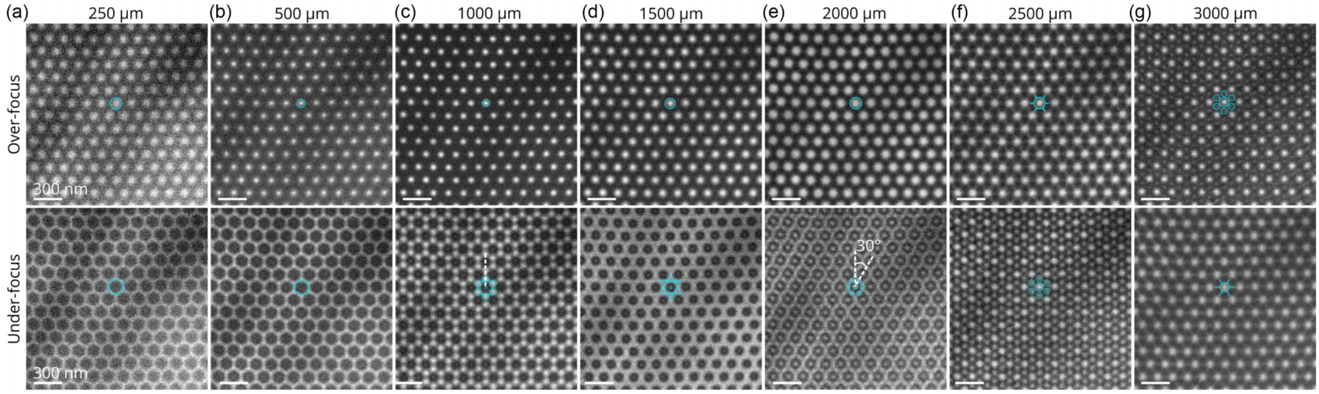

FIG. 5. Experimental Lorentz imaging of a skyrmion lattice in an FeGe sample as a function of the defocus. A circle is used to mark the position of the skyrmion and adjacent characteristic bright features in each image. Defocus distances are labeled at the top of each column. The pattern or shape of the skyrmions is marked in each image. The hexagonal skyrmion lattice in (e) is rotated by 30° relative to that in (c) under under-focus conditions. A 64 mT magnetic field is applied perpendicular to the sample. The sample thickness is approximately 120 nm. Images are recorded at a sample temperature of 250 K.

pattern observed at −1000 μm. At −2500 μm [Fig. 5(f)], the center of a skyrmion becomes the brightest region, although with weaker intensity than in the over-focus regime. Finally, at −3000 μm [Fig. 5(g)], the peripheral spots evolve into bright lines connecting neighboring skyrmions.

It is worth to note that the images at $\Delta f = -2500$ μm and +3000 μm, as well as those at −3000 μm and +2500 μm, exhibit striking similarity [Figs. 5(f) and 5(g)]. The defocus-dependent contrast and appearance of skyrmions arise from the changing interference conditions of the transmitted electron waves during Fresnel propagation, which can introduce imaging artifacts that are not related to intrinsic variations of the magnetic structure.

Simulated Lorentz imaging of the skyrmion lattice. To investigate the origin of these effects, we performed micromagnetic simulations of skyrmion lattices and calculated Lorentz TEM images as a function of the defocus distance. In addition, in order to consider effects from the sample thickness and magnetic field, we also simulated samples with a thickness of 70, 90, and 180 nm at both 150 mT and 0 mT. Note that a zero field skyrmion lattice could be obtained experimentally through field cooling [36] or electric currents [37].

For samples with a thickness of 70 and 90 nm, the simulated skyrmion patterns and contrast variations with the defocus distance show qualitative agreement with the experimental observations [see Figs. 5 and 6(a) and 6(b)]. In the 180-nm-thick sample, it is clear that the skyrmion pattern changes dramatically as a function of the defocus distance in both over- and under-focus regimes. This is partly due to a larger phase for a thicker sample as the skyrmion is longer in the thickness direction. This suggests that the magnitude of the phase also determines the optimal defocus distance for Lorentz imaging. The symmetry of the pattern as a function of the defocus distance will be discussed below.

To monitor the evolution of the contrast of skyrmions in Lorentz TEM images, we extract the intensity variation of the positions along the gray solid line indicated in Fig. 6(a), as a function of the defocus distance; see Fig. 7(a). In particular, we pick two representative positions (marked in the first column of Fig. 6) in the skyrmion lattice: skyrmion center (1), the center between two adjacent skyrmions (2). We trace their intensity variations as a function of the defocus distance, as plotted in Fig. 7(b).

From the intensity map shown in Fig. 7(a), it is seen that the map displays a periodic pattern, with a half period between position "1" and "2." In the over-focus regime, maximum intensity is located at a defocus distance between 600 and 1600 μm around the skyrmion center, with a peak at 1000 μm [see the cyan profile in Fig. 7(b)]. In the under-focus regime, the minimum intensity is also localized at the skyrmion center, though at a defocus distance between 1000 and 1600 μm, with a peak at 1500 μm [see the purple profile in Fig. 7(b)], slightly larger than that in the over-focus regime. In the center between two adjacent skyrmions, position "2," the intensity map in the over- and under-focus region shows an inverted trend compared to that of position "1." In particular, in the under-focus regime, it is clear that there are two local maxima [see the purple profile in Fig. 7(b)]. On the other hand, in the over-focus regime, between position "1" and "2," there is a localized minimum region with a defocus distance between 1800 and 2500 μm. It is worth emphasizing that the intensity at any point does not monotonically vary as a function of the defocus distance.

The intensity profiles for the two particular positions when the lattice is free of the magnetic field are also plotted in Fig. 7(b) (dashed lines). It is apparent that at a small defocus distance, the intensity difference from the lattice at 150 mT is not huge, while at high defocus distances, the difference is significant, in particular for the skyrmion center. This suggests that the magnetic field also alters the phase of the skyrmions, or the stray field also contributes to the image contrast.

We also provide similar intensity maps and intensity profiles for the 90- and 180-nm-thick samples; see Fig. S1 in the Supplemental Material [38]. It is seen that a similar behavior is also observed in the 90-nm-thick sample. On the other hand, there are considerable differences in the 180-nm-thick sample, in particular for the skyrmion center. For example, the position of the maximum intensity in the over-focus regime is shifted toward a lower defocus distance. Moreover, at a high defocus distance in the under-focus regime ($\geqslant$1500 μm), the

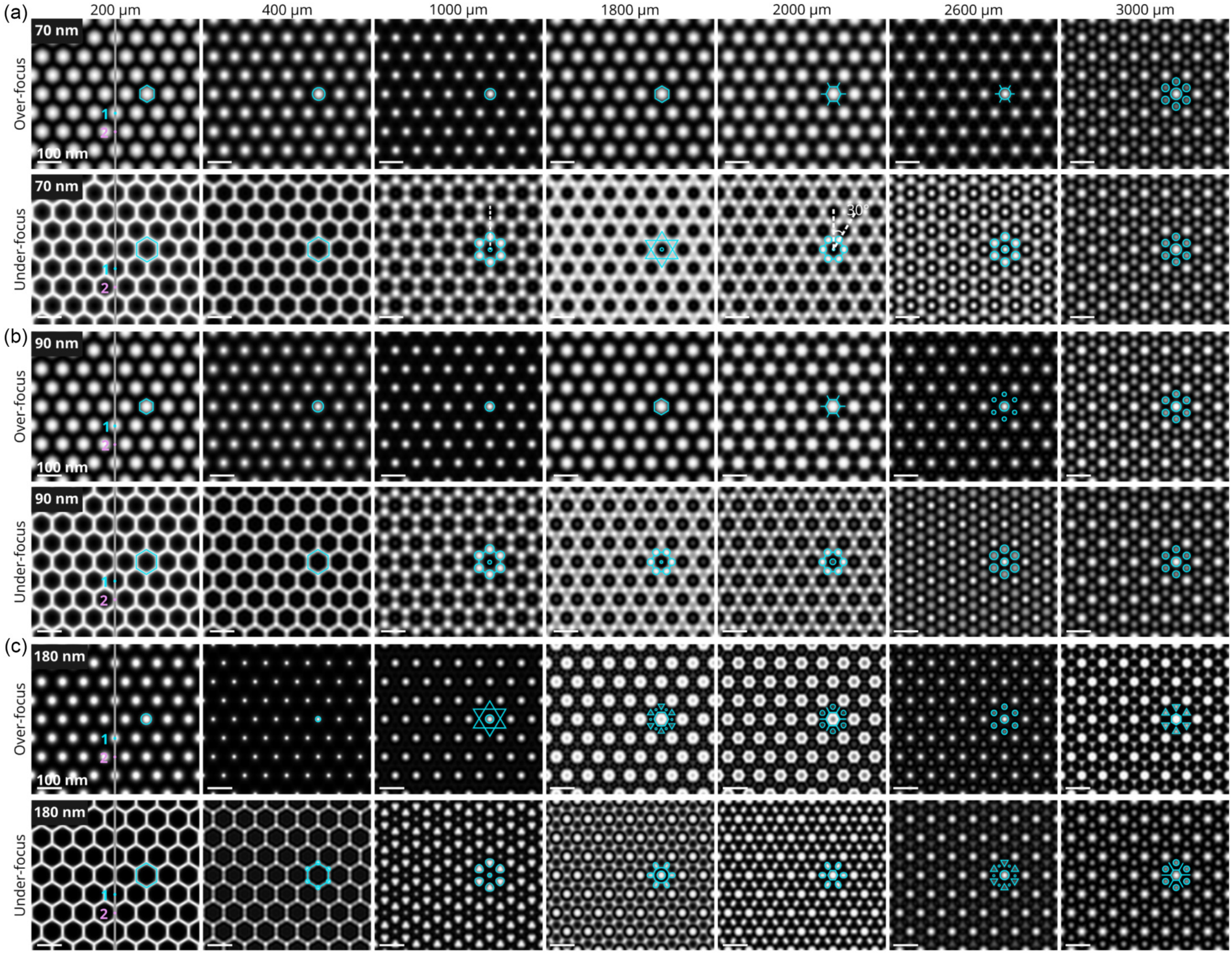

FIG. 6. Simulated Lorentz TEM images of the skyrmion lattice at different defocus distances. The sample thickness in panels (a)–(c) is 70, 90 and 180 nm, respectively. A field of 150 mT is applied perpendicular to the sample. The defocus distance is labeled on the top of each column. In the first column, gray solid lines mark the path where intensity profiles are plotted in Fig. 7. Two representative spots are also marked in cyan and purple, labeled as “1” and “2,” respectively. The pattern of the lattice is also marked.

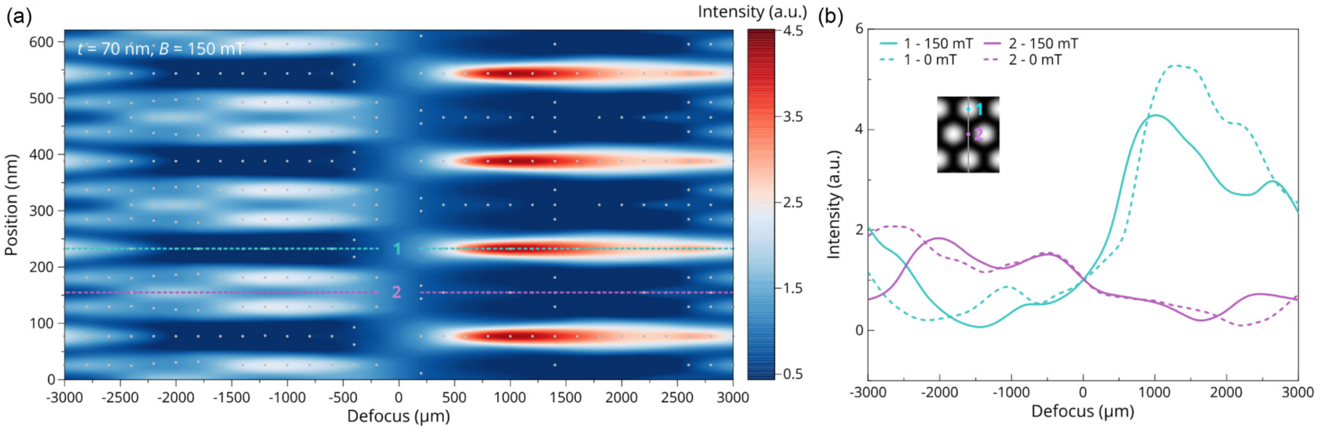

FIG. 7. Analyses of simulated Lorentz TEM images of the skyrmion lattice in the 70-nm-thick sample. (a) Intensity map for the points along the gray line [marked in Fig. 6(a)] as a function of the defocus distance. (b) Intensity profiles for the two particular points as a function of the defocus distance. “1” and “2” denote the skyrmion center and the center between two adjacent skyrmions, respectively [see the inset in (b)]. Two lines mark the positions of the two points in (a). In addition, intensity profiles for the lattice at 0 mT (dashed lines) are also plotted for comparison.

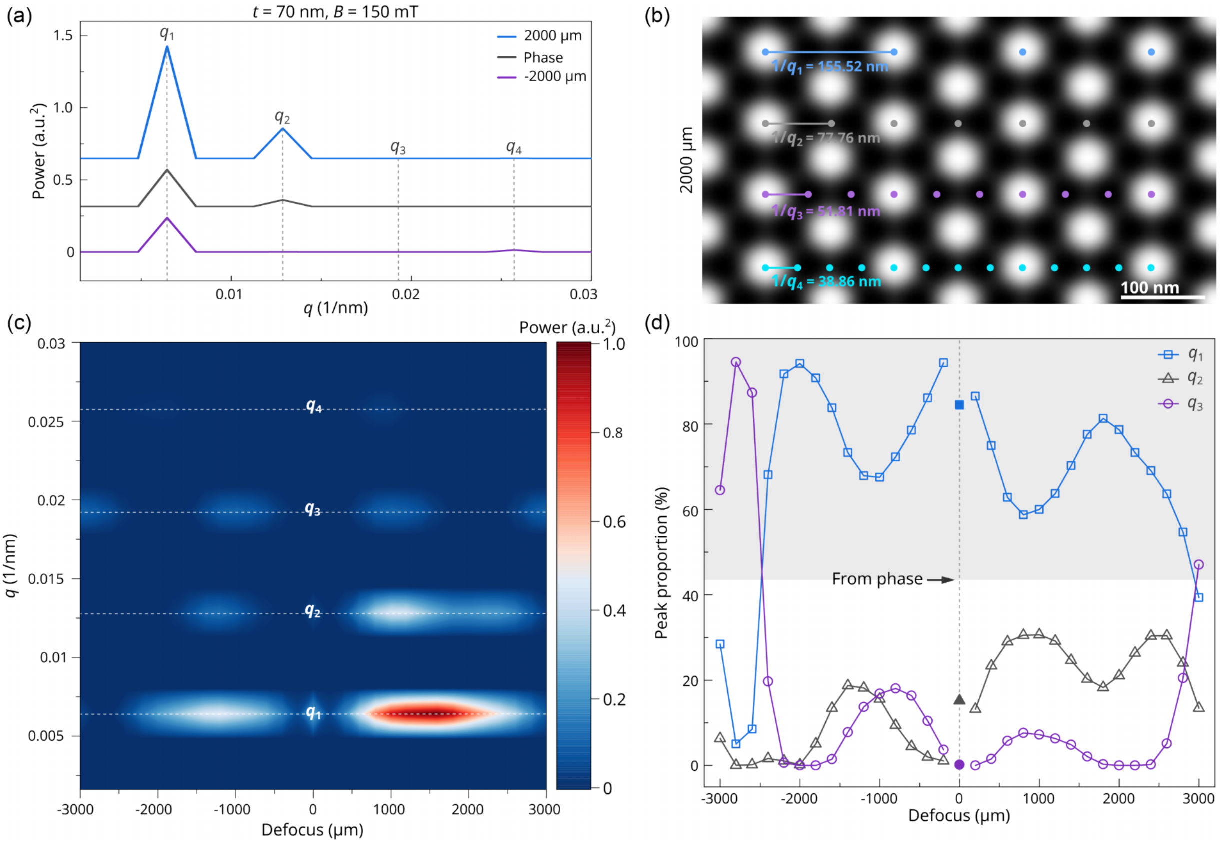

FIG. 8. Periodicity analyses of skyrmion-lattice patterns as a function of the defocus distance in the 70-nm-thick sample. (a) Representative FFT power spectra of the intensity profile along the gray line [marked in Fig. 6(a)]. The intensity profiles are from the Lorentz images at a defocus distance of 2000 μm. The FFT power spectrum of the phase is also used for comparison. The applied magnetic field is 150 mT. The characteristic peaks in the frequency domains are labeled as $\boldsymbol{q_1}$, $\boldsymbol{q_2}$, $\boldsymbol{q_3}$, and $\boldsymbol{q_4}$. Their corresponding spatial spacings are marked in (b) on the over-focus Lorentz images at a defocus distance of 2000 μm. (c) Two-dimensional FFT power spectra as a function of the defocus distance. Each vertical line in the spectrum corresponds to a similar spectrum shown in (a). The dominant peaks are localized judging from the values and labeled. (d) Evolution of the proportions of three dominant peaks (characteristic frequencies) as a function of the defocus. The dominant peaks from the phase are also plotted for comparison.

intensity of the skyrmion center shows an oscillating manner. In addition, the intensity of the skyrmion center is higher than that of the center of the two adjacent skyrmions (“2”) in the under-focus regime, whereas the situation is reversed in the other two thinner samples.

Periodicity of skyrmion-lattice patterns. From both experimental and simulated Lorentz images of the skyrmion lattice, it is clear that the hexagonal symmetry is not always maintained in the lattice, or even extra sublattices may appear in particular at a high defocus distance or the phase of skyrmion is relatively high [see Fig. 6(c)]. To further understand the evolution of the lattice pattern as a function of the defocus distance, we thus perform a fast Fourier transform (FFT) of the intensity profiles in Fig. 7(a) to analyze the frequency-domain characteristics.

Representative power spectra of the intensity profiles for Lorentz images at a defocus distance of 2000 μm and the actual phase are plotted in Fig. 8(a). It is seen that there are several peaks in the spectra, corresponding to periodic features in the frequency domain. Here we identify four major peaks in the spectra, $\boldsymbol{q_1}$, $\boldsymbol{q_2}$, $\boldsymbol{q_3}$, and $\boldsymbol{q_4}$. Their corresponding spatial spacings are marked in Fig. 8(b).

From the actual phase, the majority of the information should be localized in $\boldsymbol{q_1} = 0.00643\,\mathrm{nm}^{-1}$, 155.52 nm in real space, with a minor portion in $\boldsymbol{q_2} = \frac{1}{2}\boldsymbol{q_1} = 0.01286\,\mathrm{nm}^{-1}$, 77.76 nm in real space [see the gray profile in Fig. 8(a)]. In the over-focus Lorentz image, it is apparent that the portion of the $\boldsymbol{q_2}$ peak increases with respect to the actual phase [see the cyan profile in Fig. 8(a)]. On the other hand, in the under-focus Lorentz image, the $\boldsymbol{q_2}$ peak almost disappears, instead with another minor portion in $\boldsymbol{q_4} = \frac{1}{4}\boldsymbol{q_1} = 0.02573\,\mathrm{nm}^{-1}$, 38.86 nm in real space [see the purple profile in Fig. 8(a)]. In other Lorentz images with different defocus distances, there is an additional peak at $\boldsymbol{q_3} = \frac{1}{3}\boldsymbol{q_1} = 0.0193\,\mathrm{nm}^{-1}$, 51.81 nm in real space.

The FFT power spectra for a series of Lorentz images at varying defocus distances are thus plotted in Fig. 8(c). It is obviously seen that the four characteristic peaks change with the defocus distance. At all defocus distances, $\boldsymbol{q_1}$ is dominating in the spectra, except at a huge defocus distance ($\geqslant$2600 μm), where $\boldsymbol{q_3}$ prevails. $\boldsymbol{q_4}$ is almost negligible except at the over-focus Lorentz images with a defocus distance of around 1000 μm. It is worth noting that the $\boldsymbol{q_1}$, $\boldsymbol{q_2}$ and $\boldsymbol{q_4}$ have an asymmetric distribution with respect to the under- and over-focus regimes and dominate more in the latter, whereas the $\boldsymbol{q}_3$ shows an almost symmetric profile.

To trace the proportion of the three major peaks in the power spectra, line profiles of their proportions are plotted as a function of the defocus distance; see Fig. 8(d). Proportions of the peaks for the actual phase are also included for comparison (see solid symbols). In the phase, more than 80% of the information is localized in the $\boldsymbol{q}_1$, and the rest falls in the $\boldsymbol{q}_2$. For Lorentz images, it is clear that the localized frequency changes with the defocus distance in an oscillating and asymmetric manner in over- and under-focus regimes. At 200 μm, the over-focus Lorentz images almost display exactly the same as the actual phase. At 400 μm, the under-focus Lorentz images show a similar proportion of $\boldsymbol{q}_1$, but $\boldsymbol{q}_2$ is almost absent. This observation highlights that the optimal defocus distances for over- and under-focus Lorentz imaging are different. At a large defocus distance, $\boldsymbol{q}_3$ is dominating at both over- and under-focus regimes, suggesting that another symmetry or closed packed pattern is formed instead of the hexagonal lattice. This is consistent with experimental and simulated Lorentz images recorded at relatively large defocus distances in Figs. 5 and 6.

The FFT power spectra for the skyrmion lattice in the absence of the magnetic field are also provided in Fig. S2 [38]. Similar phenomena are also found for the frequency distributions, though no $\boldsymbol{q}_3$ dominance is found at least with a defocus distance of $\leqslant 3000$ μm. In addition, we also provide the FFT power spectra for the skyrmion lattice at 150 mT in two other thicker samples; see Fig. S3 [38]. It could be seen a similar behavior in the 90-nm-thick sample, while the situation in the 180-nm-thick sample is more complicated. In particular, there are multiple peaks (characteristic frequencies), instead of four in the thinner samples, and a mixture of at least $\boldsymbol{q}_1$ and $\boldsymbol{q}_3$ is found at high defocus distances, which may make the Lorentz images more complicated in terms of symmetry of the lattice pattern. This is also observed in simulated Lorentz images at high defocus distances; see Fig. 6(c). This suggests that for a large phase object (thick samples), a relatively small defocus is always favorable by not introducing artificial symmetry and ideally a series of Lorentz images as a function of the defocus distance is always necessary for accurate interpretation of Lorentz images, alongside support from simulated images from micromagnetic models.

In the present case, the skyrmions can be regarded as quasi-two-dimensional (2D) Bloch-type structures extending through the sample thickness. In reality, the magnetization is not perfectly uniform, and slight twisting or Néel-type surface caps may occur near the surfaces [39–43]. This scenario is different from the atomic crystal lattice, in which atoms are arranged discretely with a physical spacing along the thickness direction. Multislice simulations of high resolution TEM images for a hexagonal cobalt crystal [001] as a function of the defocus distance and specimen thickness are provided in Fig. S4 [38] for comparison.

Tomographic tilt-series imaging of the skyrmion lattice. Since the skyrmion lattice is a 2D periodic structure, it would be interesting to see the hexagon lattice at different zone axes. Tomographic tilt-series experiments on the skyrmion lattice in the FeGe sample were thus performed. Due to the fact that the magnetic field in the TEM was applied using the objective lens, in order not to destroy the skyrmion lattice in the process of the tilt, a zero-magnetic-field skyrmion lattice was obtained through the field cooling protocol. Representative Lorentz images of the skyrmion lattice as a function of the specimen tilt angles are provided in Figs. 9(a)–9(d). It is found that the symmetry of the lattice pattern is changing with the specimen tilt angle. A square-lattice structure could be seen at high tilt angles [see Figs. 9(c) and 9(d)]. A similar observation was also reported previously; see, e.g., Supplementary Fig. 3. in Ref. [36]. It is worth noting that such a square lattice could be misinterpreted as the so-called meron/antimeron lattice [16], if no information of the specimen tilt angle is provided.

A possible explanation for the changing symmetry of the lattice pattern is due to projection nature of the TEM imaging. Individual skyrmions could be assumed as cylindrical tubes. As the tilt angle increases, the circular cross section is viewed more elliptical, and the tube become longer. Inside the skyrmion lattice, these skyrmions overlap with each other and form different symmetric patterns.

To visualize how the tilt axis orientation governs the projected lattice symmetry, we performed additional simulations under different tilt configurations, as summarized in Fig. 10. The tilt axis, indicated by the white coordinate markers in the first over-focus images at a tilt angle of 0° in Figs. 10(a)–10(c), is oriented along the x axis and y axis and $+30^\circ$ from the x axis, respectively. It could be seen that experimental images in Figs. 9(e)–9(i) are in excellent agreement with simulated images in Fig. 10(c).

The present analysis considers idealized periodic lattices. In practical samples, grain boundaries between misoriented skyrmion domains can introduce distinct contrast features, especially under large defocus or tilt conditions. Such inhomogeneities may further complicate image interpretation and are an important subject for future studies.

We also have to highlight that the Lorentz image contrast is due to the 2D projection of the 3D magnetization structure. This is in particular crucial for the 3D magnetic structures that could not be assumed to be 2D spin textures, e.g., antiskyrmions in cubic chiral magnets [13]. Such twisted magnetization textures in antiskyrmions along the thickness direction produces a circular-ring contrast (depending on the sample thickness) in the Lorentz images, mimicking similar features from skyrmionium textures. However, these two textures are completely different. Moreover, chiral bobbers and dipole strings are also not distinguishable from Lorentz images, though they have different numbers of Bloch points [15,44]. This highlights the fact that for complicated 3D magnetic textures, it is not straightforward to tell the magnetization configurations only from Lorentz TEM images. Complementary information including from experiments and theory is necessary for reliable interpretations.

V. CONCLUSIONS

In this work, we have systematically investigated the Lorentz image contrast for individual skyrmions, two neighboring skyrmions, and the skyrmion lattice as a function of the defocus distance and the specimen tilt. We also discuss the effects from the applied external magnetic field and the sample thickness. We analyze the image contrast through the

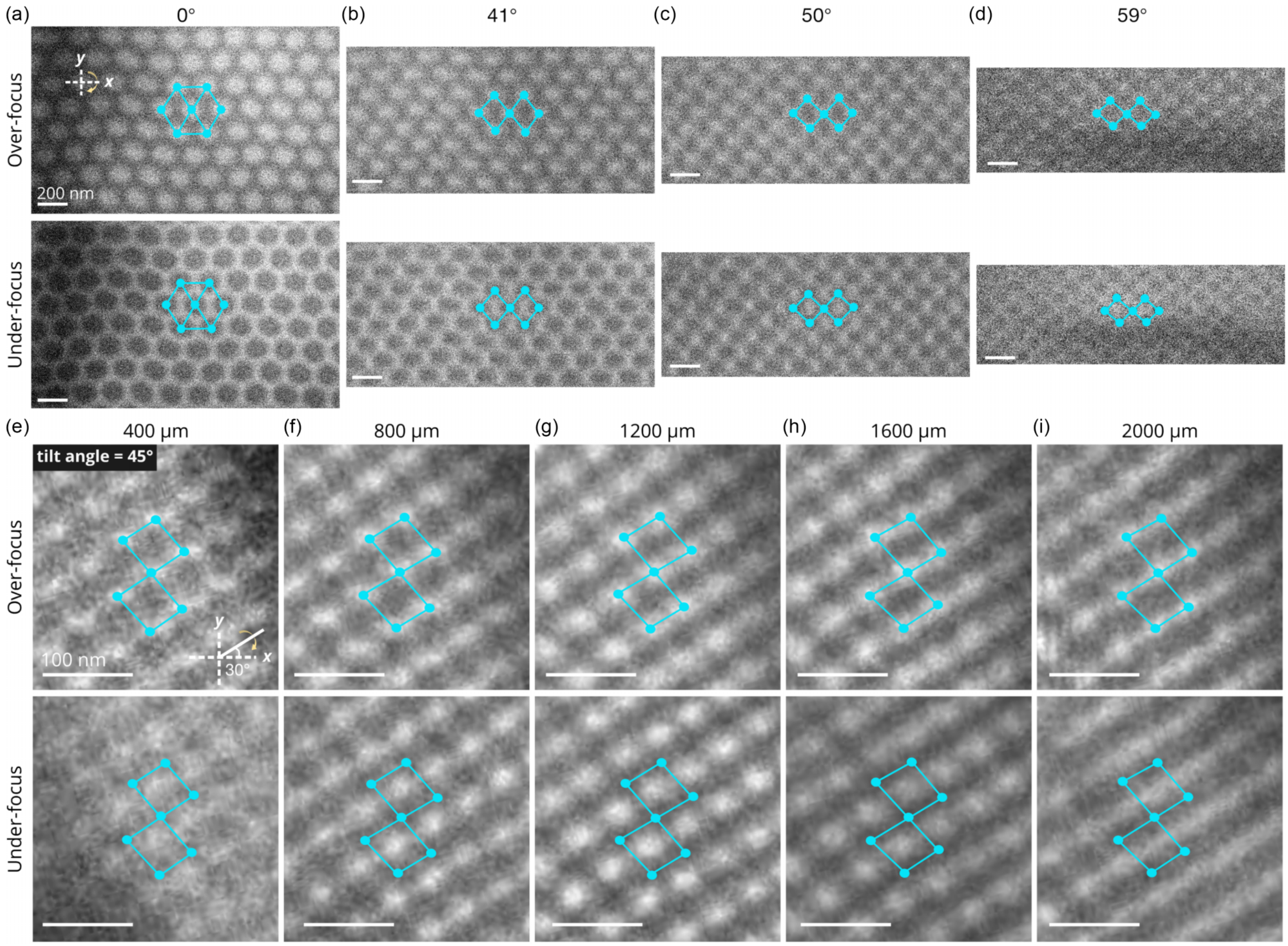

FIG. 9. Representative experimental Lorentz TEM images of the skyrmion lattice in an FeGe sample under different specimen tilt angles and defocus distances. (a–d) Images recorded with the tilt axis along the x direction at various tilt angles, as indicated above each column. The defocus distance for all images is 400 μm. (e)–(i) Additional images acquired with the tilt axis rotated by $+30^\circ$ from the x axis, the tilt angle is 45°, and defocus distances systematically varied from 400 μm to 2000 μm. The defocus distance is marked at the top row of (e)–(i). The symmetry of the skyrmion lattice at each image is marked. The sample thickness is approximately 180 nm, and no external magnetic field is applied.

intensity profiles and periodicity in the lattice patterns. It should be concluded that a relatively small defocus distance would not create artifacts albeit at the expense of the magnitude of the contrast from skyrmions. The acquisition of a series of Lorentz images as a function of the defocus distance is strongly suggested in experiments for accurate interpretations, alongside support from simulated Lorentz images from the magnetization textures in the micromagnetic calculations. Due to the projection nature of the TEM imaging, this is crucially important for the complicated 3D magnetic objects.

While our study focuses on Bloch-type skyrmions and Fresnel-mode imaging, the underlying principles and challenges are applicable to broader phase contrast techniques. Electrostatic artifacts, beam effects, specimen preparation, and inhomogeneous textures (e.g., grain boundaries or Néel components) may further complicate contrast interpretation. We hope that our findings will contribute to a growing awareness of artifact sources and motivate robust imaging protocols across various topological magnetic systems.

ACKNOWLEDGMENTS

X.C., D.Y., and F.Z. acknowledge financial support from the National Key R&D Program of China (Grant No. 2024YFA1611100), the National Natural Science Fund for Excellent Young Scientists Fund Program (Overseas) and the General Program (Grant No. 52373226), and the Fundamental Research Funds for the Central Universities. F.Z. is grateful to the GJYC program of Guangzhou (No. 2024D01J0060), the Guangzhou Basic and Applied Basic Research Foundation (No. SL2024A04J00852), the Guangdong Provincial Quantum Science Strategic Initiative (Grant No. GDZX2401002), and the Xiaomi Young Talents Program. A.S. and N.S.K. acknowledge financial support from the Deutsche Forschungsgemeinschaft through SPP 2137 "Skyrmionics" Grant No. KI 2078/1-1. L.Y. acknowledges financial support from the Beijing Natural Science Foundation (Grant No. 2252029) and the National Natural Science Foundation of China (Grant No. 52204379). R.E.D-B. is grateful for financial support from the Deutsche Forschungsgemeinschaft (Project-ID 405553726-TRR 270). This project has

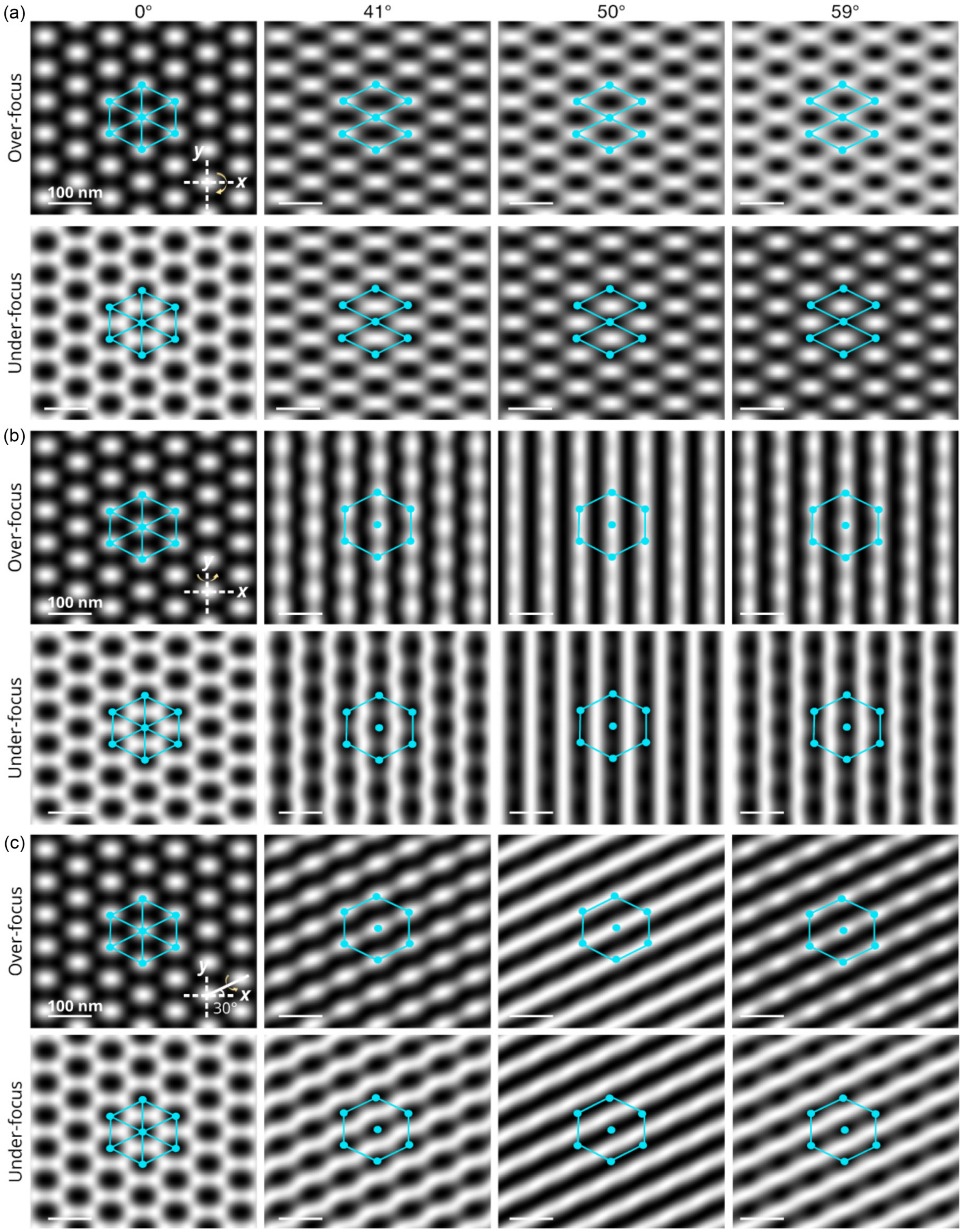

FIG. 10. Simulated Lorentz TEM images of a Bloch-type skyrmion lattice as a function of the specimen tilt angles and axes. The corresponding tilt angles are indicated above each column. In (a)–(c) the tilt axis (shown by white coordinate markers in the over-focus images at 0° tilt) is oriented along the x axis, y axis, and $+30^\circ$ from the x axis, respectively. The sample thickness is 180 nm. The applied magnetic field is 150 mT. The defocus distance for all images is 1200 μm. The sample thickness is 180 nm. The lattice pattern is also marked in each image.

received funding from the European Research Council under the European Union's Horizon 2020 Research and Innovation Programme (Grant No. 856538, project "3D MAGiC").

The authors have no conflicts of interest to disclose.

DATA AVAILABILITY

The data that support the findings of this article are available from the authors upon reasonable request.

[1] I. Manke, N. Kardjilov, R. Schäfer, A. Hilgerand, M. Strobl, M. Dawson, C. Grünzweig, G. Behr, M. Hentschel, C. David, A. Kupsch, A. Lange, and J. Banhart, Three-dimensional imaging of magnetic domains, Nat. Commun. **1**, 125 (2010).

[2] O. Kazakova, R. Puttock, C. Barton, H. Corte-León, M. Jaafar, V. Neu, and A. Asenjo, Frontiers of magnetic force microscopy, J. Appl. Phys. **125**, 060901 (2019).

[3] X. W. Chen, R. Adam, D. E. Bürgler, F. Z. Wang, Z. Y. Lu, L. N. Pan, S. Heidtfeld, C. Greb, M. H. Liu, Q. F. Liu, J. B. Wang, C. M. Schneider, and D. R. Cao, Ultrafast demagnetization in ferromagnetic materials: Origins and progress, Phys. Rep. **1102**, 1 (2025).

[4] P. Fischer, X-ray imaging of magnetic structures, IEEE Trans. Magn. **51**, 1 (2014).

[5] C. Phatak, A. K. Petford-Long, and M. De Graef, Recent advances in Lorentz microscopy, Curr. Opin. Solid State Mater. Sci. **20**, 107 (2016).

[6] A. Kovács and R. E. Dunin-Borkowski, Magnetic imaging of nanostructures using off-axis electron holography, in *Handbook of Magnetic Materials* (Elsevier, Delft, 2018), Vol. 27, pp. 59–153.

[7] S. Toyama, T. Seki, Y. Kohno, Y. O. Murakami, Y. Ikuhara, and N. Shibata, Nanoscale electromagnetic field imaging by advanced differential phase-contrast STEM, Nat. Rev. Electr. Eng. **2**, 27 (2025).

[8] M. de Graef, Lorentz microscopy: Theoretical asis and image simulations, in *Magnetic Imaging and Its Applications to Materials*, Experimental Methods in the Physical Sciences Vol. 36, edited by M. De Graef and Y. Zhu (Academic Press, 2001), pp. 27–67.

[9] Y. M. Zhu, *Modern Techniques for Characterizing Magnetic Materials*, Springer Ebook Collection/Chemistry and Materials Science 2005–2008 (Springer US, New York, 2005).

[10] P. J. Grundy and S. R. Herd, Lorentz microscopy of bubble domains and changes in domain wall state in hexaferrites, Phys. Stat. Sol. (a) **20**, 295 (1973).

[11] X. Z. Yu, Y. Onose, N. Kanazawa, J. H. Park, J. H. Han, Y. Matsui, N. Nagaosa, and Y. Tokura, Real-space observation of a two-dimensional skyrmion crystal, Nature (London) **465**, 901 (2010).

[12] A. K. Nayak, V. Kumar, T. Ma, P. Werner, E. Pippel, R. Sahoo, F. Damay, U. K. Rößler, C. Felser, and S. S. P. Parkin, Magnetic antiskyrmions above room temperature in tetragonal Heusler materials, Nature (London) **548**, 561 (2017).

[13] F. Zheng, N. S. Kiselev, L. Yang, V. M. Kuchkin, F. N. Rybakov, S. Blügel, and R. E. Dunin-Borkowski, Skyrmion–antiskyrmion pair creation and annihilation in a cubic chiral magnet, Nat. Phys. **18**, 863 (2022).

[14] X. Z. Yu, Y. Tokunaga, Y. Kaneko, W. Z. Zhang, K. Kimoto, Y. Matsui, Y. Taguchi, and Y. Tokura, Biskyrmion states and their current-driven motion in a layered manganite, Nat. Commun. **5**, 3198 (2014).

[15] F. Zheng, F. N. Rybakov, A. B. Borisov, D. Song, S. Wang, Z.-A. Li, H. Du, N. S. Kiselev, J. Caron, A. Kovács, M. Tian, Y. Zhang, S. Blügel, and R. E. Dunin-Borkowski, Experimental observation of chiral magnetic bobbers in B20-type FeGe, Nat. Nanotechnol. **13**, 451 (2018).

[16] X. Z. Yu, W. Koshibae, Y. Tokunaga, K. Shibata, Y. Taguchi, N. Nagaosa, and Y. Tokura, Transformation between meron and skyrmion topological spin textures in a chiral magnet, Nature (London) **564**, 95 (2018).

[17] F. Zheng, N. S. Kiselev, F. N. Rybakov, L. Y. Yang, W. Shi, S. Blügel, and R. E. Dunin-Borkowski, Hopfion rings in a cubic chiral magnet, Nature (London) **623**, 718 (2023).

[18] J. C. Loudon, A. C. Twitchett-Harrison, D. Cortés-Ortuño, M. T. Birch, L. A. Turnbull, A. Štefančič, F. Y. Ogrin, E. O. Burgos-Parra, N. Bukin, A. Laurenson, H. Popescu, M. Beg, O. Hovorka, H. Fangohr, P. A. Midgley, G. Balakrishnan, and P. D. Hatton, Do images of biskyrmions show type-ii bubbles? Adv. Mater. **31**, 1806598 (2019).

[19] Y. Yao, B. Ding, J. Cui, X. Shen, Y. G. Wang, W. H. Wang, and R. C. Yu, Magnetic hard nanobubble: A possible magnetization structure behind the bi-skyrmion, Appl. Phys. Lett. **114**, 102404 (2019).

[20] S. McVitie, S. Hughes, K. Fallon, S. McFadzean, D. McGrouther, M. Krajnak, W. Legrand, D. Maccariello, S. Collin, K. Garcia, N. Reyren, V. Cros, A. Fert, K. Zeissler, and C. H. Marrows, A transmission electron microscope study of Néel skyrmion magnetic textures in multilayer thin film systems with large interfacial chiral interaction, Sci. Rep. **8**, 5703 (2018).

[21] T. Denneulin, J. Caron, M. Hoffmann, M. Lin, H. K. Tan, A. Kovács, S. Blügel, and R. E. Dunin-Borkowski, Off-axis electron holography of Néel-type skyrmions in multilayers of heavy metals and ferromagnets, Ultramicroscopy **220**, 113155 (2021).

[22] Y. Yao, B. Ding, J. J. Liang, H. Li, X. Shen, R. C. Yu, and W. H. Wang, Chirality flips of skyrmion bubbles, Nat. Commun. **13**, 5991 (2022).

[23] J. Cui, Y. Yao, X. Shen, Y. G. Wang, and R. C. Yu, Artifacts in magnetic spirals retrieved by transport of intensity equation (TIE), J. Magn. Magn. Mater. **454**, 304 (2018).

[24] Y. Aharonov and D. Bohm, Significance of electromagnetic potentials in the quantum theory, Phys. Rev. **115**, 485 (1959).

[25] L. Reimer, *Transmission Electron Microscopy: Physics of Image Formation and Microanalysis* (Springer, Berlin, 2013).

[26] C. B. Carter and D. B. Williams, *Transmission Electron Microscopy: Diffraction, Imaging, and Spectrometry* (Springer International Publishing, Cham, 2016).

[27] F. N. Rybakov and E. Babaev, Excalibur software, http://quantumandclassical.com/excalibur/.

[28] A. R. C. McCray, T. Cote, Y. Li, A. K. Petford-Long, and C. Phatak, Understanding complex magnetic spin textures with simulation-assisted Lorentz transmission electron microscopy, Phys. Rev. Appl. **15**, 044025 (2021).

[29] J. Barthel, Dr. Probe: A software for high-resolution STEM image simulation, Ultramicroscopy **193**, 1 (2018).

[30] M. Beleggia, M. A. Schofield, V. V. Volkov, and Y. Zhu, On the transport of intensity technique for phase retrieval, Ultramicroscopy **102**, 37 (2004).

[31] J. A. Garlow, S. D. Pollard, M. Beleggia, T. Dutta, H. Yang, and Y. Zhu, Quantification of mixed Boch-Néel topological spin textures stabilized by the Dzyaloshinskii-Moriya interaction in Co/Pd multilayers, Phys. Rev. Lett. **122**, 237201 (2019).

[32] A. O. Leonov, T. L. Monchesky, J. C. Loudon, and A. N. Bogdanov, Three-dimensional chiral skyrmions with attractive interparticle interactions, J. Phys.: Condens. Matter **28**, 35LT01 (2016).

[33] X. S. Wang, H. Y. Yuan, and X. R. Wang, A theory on skyrmion size, Commun. Phys. **1**, 31 (2018).

[34] H. Wu, X. Hu, K. Jing, and X. R. Wang, Size and profile of skyrmions in skyrmion crystals, Commun. Phys. **4**, 210 (2021).

[35] J. Iwasaki, M. Mochizuki, and N. Nagaosa, Universal current-velocity relation of skyrmion motion in chiral magnets, Nat. Commun. **4**, 1463 (2013).

[36] X. Yu, D. Morikawa, T. Yokouchi, K. Shibata, N. Kanazawa, F. Kagawa, T.-h. Arima, and Y. Tokura, Aggregation and collapse dynamics of skyrmions in a non-equilibrium state, Nat. Phys. **14**, 832 (2018).

[37] X. B. Zhao, J. Tang, K. Pei, W. W. Wang, S. Lin, H. F. Du, M. L. Tian, and R. C. Che, Current-induced magnetic skyrmions with controllable polarities in the helical phase, Nano Lett. **22**, 8793 (2022).

[38] See Supplemental Material at http://link.aps.org/supplemental/10.1103/sm5r-2vps for additional analyses of simulated Lorentz TEM data, including defocus-dependent intensity mapping of the skyrmion-lattice contrast for different sample thicknesses; Fourier analysis of the skyrmion-lattice periodicity in a 70-nm-thick sample at 0 mT as a function of defocus; Fourier analysis of the skyrmion-lattice periodicity and characteristic frequency evolution in thicker samples at 150 mT; and multislice simulations of high-resolution TEM images of hexagonal cobalt crystals with varying thickness and defocus.

[39] F. N. Rybakov, A. B. Borisov, and A. N. Bogdanov, Three-dimensional skyrmion states in thin films of cubic helimagnets, Phys. Rev. B **87**, 094424 (2013).

[40] F. N. Rybakov, A. B. Borisov, S. Blügel, and N. S. Kiselev, New spiral state and skyrmion lattice in 3D model of chiral magnets, New J. Phys. **18**, 045002 (2016).

[41] S. L. Zhang, G. van der Laan, W. W. Wang, A. A. Haghighirad, and T. Hesjedal, Direct observation of twisted surface skyrmions in bulk crystals, Phys. Rev. Lett. **120**, 227202 (2018).

[42] S. Schneider, D. Wolf, M. J. Stolt, S. Jin, D. Pohl, B. Rellinghaus, M. Schmidt, B. Büchner, S. T. B. Goennenwein, K. Nielsch, and A. Lubk, Induction mapping of the 3D-modulated spin texture of skyrmions in thin helimagnets, Phys. Rev. Lett. **120**, 217201 (2018).

[43] W. Legrand, J. Chauleau, D. Maccariello, N. Reyren, S. Collin, K. Bouzehouane, N. Jaouen, V. Cros, and A. Fert, Hybrid chiral domain walls and skyrmions in magnetic multilayers, Sci. Adv. **4**, eaat0415 (2018).

[44] A. S. Savchenko, F. Zheng, N. S. Kiselev, L. Yang, F. N. Rybakov, S. Blügel, and R. E. Dunin-Borkowski, Diversity of states in a chiral magnet nanocylinder, APL Mater. **10**, 061110 (2022).